MICROSTRUCTURE OF CR2O3 COATINGS ON STEEL AND THE EFFECT OF SILICON

VANDENBURG, M; DEHOSSON, JTM; Burg, M. van den

Published in:
Journal of materials research

Publication date:
1994

Microstructure of Cr_2O_3 coatings on steel and the effect of silicon

M. Van den Burg and J. Th. M. De Hosson
Department of Applied Physics, University of Groningen, Nijenborgh 4, 99747AG Groningen, The Netherlands

(Received 12 March 1993; accepted 24 August 1993)

This paper concentrates on the microstructural features of steel containing 22 wt. % Cr, coated with Cr_2O_3 by laser processing. It turned out that after laser coating the Cr_2O_3 powder has completely transformed to $Fe_{0.3}Cr_{2.7}O_4$ having the tetragonal distorted spinel structure. Dispersed in the coating are metallic particles with composition FeCr and a bcc structure. The phases in the coating can be explained from the Fe–Cr–O equilibrium phase diagram with the assumption that complete phase equilibrium is reached in the liquid state but not during solidification. The two equilibrium phases, L_o and L_m, that exist in the molten state solidify as two independent liquids. Addition of Si to the ceramic material, either from the steel matrix or from the ceramic powder, results in a dendritic solidification structure of Cr_3O_4 dendrites and a Si-containing glassy phase. The dendrites are oriented vertically in the coating, resembling the columnar microstructure that is also observed in ZrO_2 thermal barrier coatings. This structure contains fewer microcracks parallel to the interface resulting in a mechanically more stable ceramic coating.

I. INTRODUCTION

Ceramic coatings on metals offer a method to improve the mechanical, thermal, and chemical properties of surfaces while maintaining the good bulk properties of the metal. To improve the physical properties at the highest loaded positions, laser processing can play an important role because of the very localized character of the laser melting process. If the laser is combined with an experimental setup feeding ceramic powder at the melt pool, ceramic coatings can be applied locally without changing the bulk of the material.

Another advantage of laser coating is the very high temperature which can be attained during laser treatment. This makes it possible to completely melt a ceramic material. Interaction between the laser melt pool and the molten ceramic can result in reactions between the metal and the ceramic, resulting in a better wetting and a stronger interface between the metal and the ceramic. This process does require an appropriate knowledge of the starting materials and the reactions that may take place.

II. EXPERIMENTAL

A CW–CO_2-laser (Spectra Physics 820) was used for coating substrate material with a ceramic layer. The operating conditions were 1.0 kW laser power, a spot size of 0.75 mm, and a laser scan velocity of 20 mm/s. The overlap between subsequent laser tracks was 75%. Cr_2O_3 powder was delivered at the melt pool by means of a homemade powder feeding system optimized for the low feed rates needed for laser coating. The powders used were Cr_2O_3-powder and Cr_2O_3-powder containing 5 wt. % SiO_2. The size distribution of both powders peaked around 10 μm. As substrate, a single phase bcc alloy containing 78 wt. % Fe and 22 wt. % Cr (Fe_4Cr) and a dual phase duplex SAF2205 steel were used, the chemical composition of which is listed in Table I. Color etching and x-ray diffraction methods indicate the duplex steel is still dual phase after the laser treatment (Fig. 1). The ratio of α–Fe to γ–Fe was not changed by the laser treatment, but the average grain size was reduced due to the high cooling rates during laser treatment.

X-ray diffraction was used to identify the phases present at different depths in the laser coating. The peak positions of the Cr_3O_4 phase[2] were used to calculate deviations from the lattice parameters of the perfect Cr_3O_4 structure. Cross-sectional SEM and optical microscopy were applied to study the solidification structures in the laser track and in the ceramic coating. Etching with modified Groesbeck's reagent[3] was found suitable to reveal the microstructure of the ceramic coating.

Cross-sectional TEM was used to identify phases and orientation relations within the coating and between the metal and the coating. Cross-sectional TEM specimens were prepared by gluing two ceramic surfaces using a two component epoxy and subsequently cutting them into rectangles small enough to fit into

TABLE I. Chemical composition (nominal) of duplex SAF 2205 (wt. %).[1]

C	Si	Mn	Cr	Ni	Mo
0.03	1.0	2.0	22	5.5	3.0

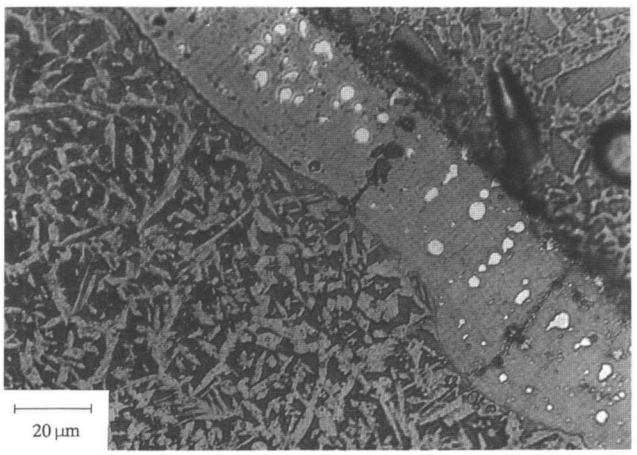

FIG. 1. Color-etched X-section of the laser track on duplex SAF 2205. Ferrite colored, austenite not attacked. Etched using Lichtenegger and Bloech color etchant (LB1).

a 3 mm specimen holder. The specimens were dimpled to a thickness of about 40 μm and thinned by ion milling afterward. The composition of the different phases was analyzed using EDS (energy dispersive x-ray spectroscopy).

III. RESULTS

A. Chemical composition of the coating

X-ray diffraction, as well as electron diffraction, indicated that the coating consisted of Cr_3O_4 having the distorted spinel-type structure. This structure is basically the spinel structure, but indexing of planes and directions is affected by a rotation of the A- and the B-axis by 45° with respect to the normal spinel. According to the x-ray diffraction measurements (Fig. 2), the addition of 4 at. % Fe and 1.5 at. % Mn resulted in elongated lattice parameters. An x-ray diffraction crystallography program[4] calculated that A changes from 0.6145 nm to 0.6161 nm and C changes from 0.755 nm to 0.776 nm. In x-ray diffraction it was observed that the $(004)_{Cr_3O_4}$ peak is broadened, pointing at a variation in the C-parameter: $0.765 < C < 0.778$ nm.

EDS (energy dispersive spectrometry of x-rays) indicated a ratio of Cr : Fe being 9 : 1 resulting in a chemical formula of $Fe_{0.3}Cr_{2.7}O_4$. In the case of the SAF 2205 matrix, 1.5 at. % Mn could be detected in the coating. Near the surface of the coating Cr_2O_3 was detected (Fig. 3), and over a distance of 5 μm the Cr : Fe ratio changed to 12 : 1, indicating insufficient reaction times. The shorter reaction times were due to the powder feeding system. It delivered powder at the rear of the melt pool where the coating was already solidifying.

In the coating dispersed metallic particles were observed with an average composition of $Fe_{0.5}Cr_{0.5}$ and a bcc structure. The ratio of the Cr over Fe content was found to vary by as much as 10%. The variation in the Fe to Cr content is accompanied by the small local compositional changes in the Cr_3O_4 mentioned above.

In case the matrix material or the coating powder contained silicon, a glassy phase containing Cr and Si in a ratio 1 : 1 was observed. This phase formed interdendritically during the formation of the Cr_3O_4. Cr_3O_4 particles were also found in the laser-melted steel matrix, all having a spherical shape. The composition of

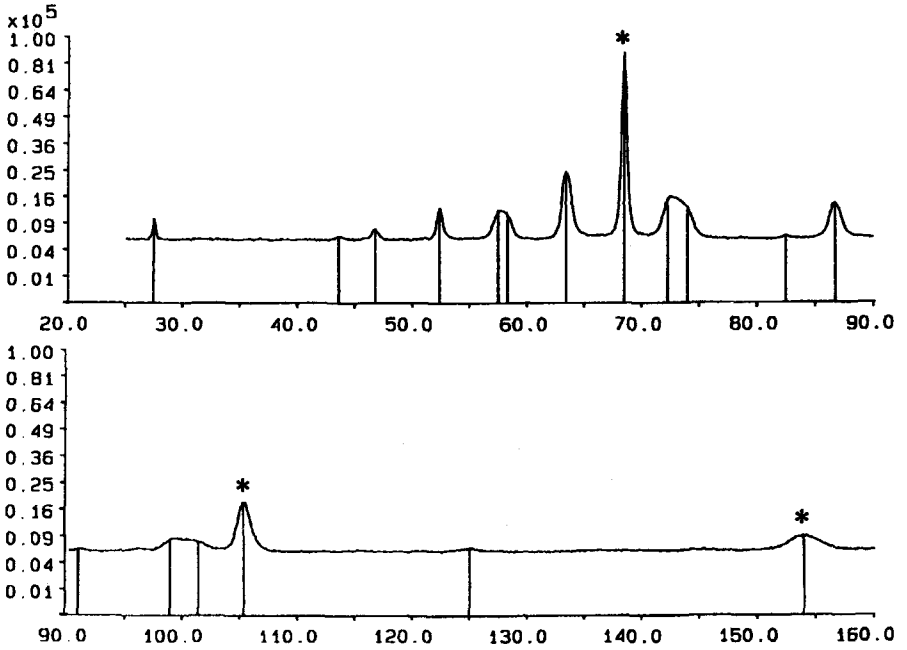

FIG. 2. X-ray diffractogram of Cr_3O_4 coating on the duplex showing α–FeCr (*) and Cr_3O_4 (other peaks) phases.

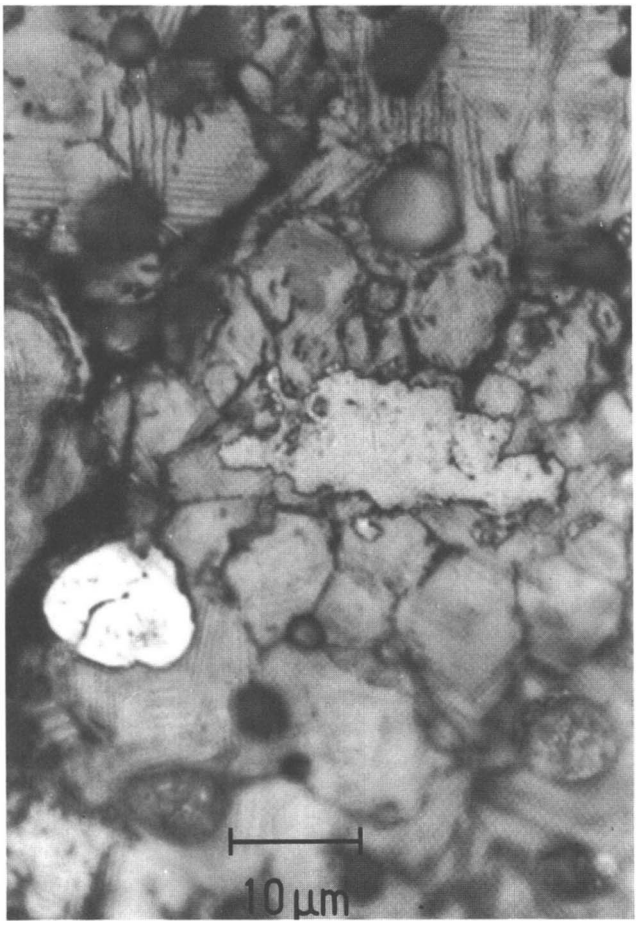

FIG. 3. X-section of Cr_3O_4 coating on duplex SAF 2205. Irregular light gray patch is a primary Cr_2O_3 particle. White particle is α–FeCr.

these particles was the same as the composition of the ceramic coating with a chemical formula of $Fe_{0.3}Cr_{2.7}O_4$.

B. Microstructure of Cr_3O_4 coating on Fe_4Cr without Si

In addition to the macrocracks which were always found to be present regardless of the substrate used, etching revealed that the coating was full of microcracks (Fig. 4).

TEM showed that the orientation of the ceramic in the coating was nearly constant over very long distances (100 μm). Small orientation changes were observed over distances of a few μm (Fig. 5). Part of the orientation change was localized in a defect wall structure and part was due to the cumulative effect of faults and twins within the cells. Sometimes microcracks could be observed running through the Cr_3O_4.

A microstructure containing very fine dispersed FeCr particles was observed. The size of the FeCr particles was typically less than 1 μm and the shape of the particles was spherical or elliptical. The FeCr particles were randomly dispersed in the coating.

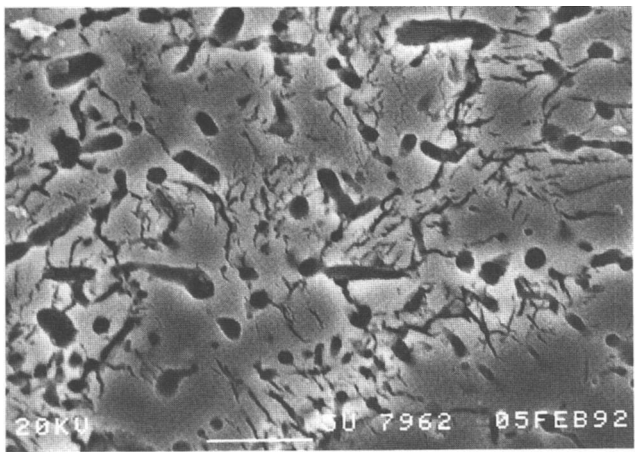

FIG. 4. Etched X-section of Cr_3O_4 coating on Fe 22 wt. % Cr showing microcracks. Holes are due to etching of FeCr particles. Etched in modified Groesbeck.

They all consisted of a single grain bcc FeCr. These FeCr particles all have the following orientation relationship with the surrounding Cr_3O_4 (Fig. 6): $(110)_{Cr_3O_4} // (200)_{FeCr}$ and $[\bar{1}12]_{Cr_3O_4} // [001]_{FeCr}$. This is in agreement with earlier results.[5] No orientation relationship was observed between the bcc matrix and the Cr_3O_4 coating, indicating separate solidification histories for the matrix and the coating.

C. Microstructure of Cr_3O_4 coating on duplex with Si

Etching revealed a dendritic growth structure existing in the ceramic coating (Fig. 7). These dendrites all seemed to originate from a very thin homogeneous Cr_3O_4 layer at the interface having a thickness of 2 to 5 μm. Over almost the entire width of the laser track the dendrites were almost vertical, except for a tilt of about 10° in the direction of the beam movement. At the

FIG. 5. Dark-field TEM image of Cr_3O_4 coating on Fe 22 wt. % Cr showing a very fine twinned structure.

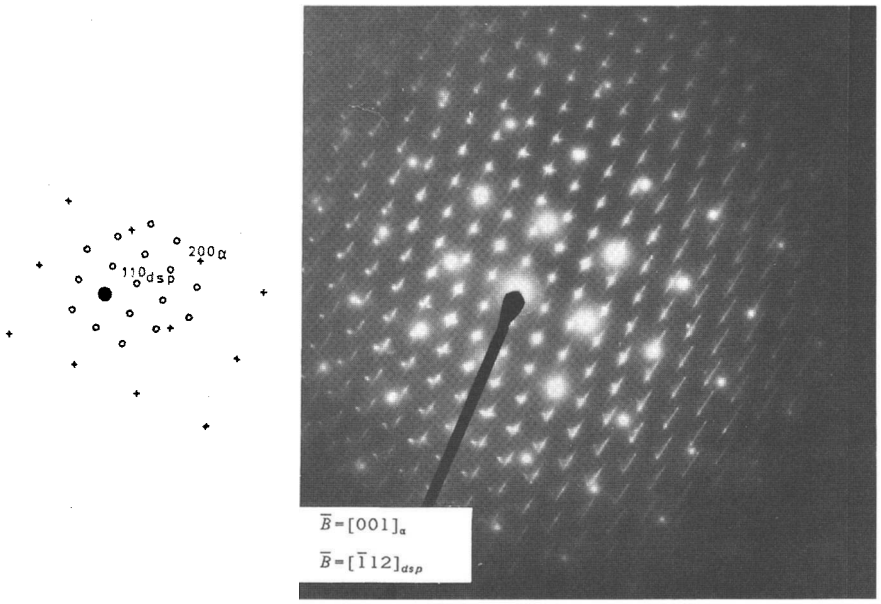

FIG. 6. Electron diffraction pattern of the FeCr particle (α) in Cr_3O_4 (dsp) coating showing the orientation relationship of $(110)_{Cr_3O_4}$ // $(200)_{FeCr}$ and $[\bar{1}12]_{Cr_3O_4}$ // $[001]_{FeCr}$.

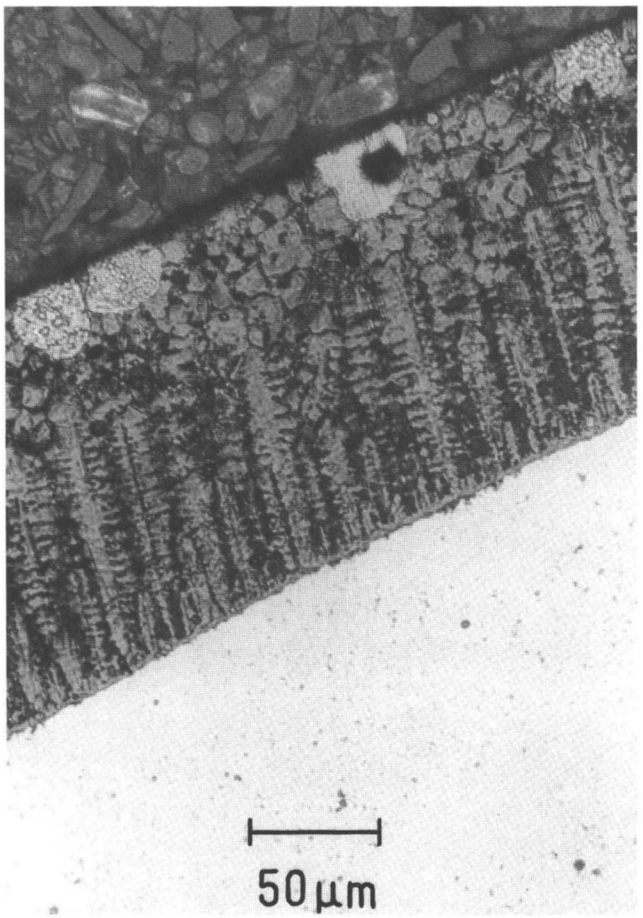

FIG. 7. Etched longitudinal section of Cr_3O_4 coating on duplex SAF 2205 showing dendrites. Etched in modified Groesbeck.

edges of the laser pool, the dendrites were tilted over larger angles. Only the primary arms of the dendrites were fully developed. The spacing between the dendrites can vary, but is typically between 10 and 20 μm. The dendrites broadened to the top of the coating.

At a variable distance from the interface, in the range of 30 to 80 μm, the dendrites were oriented differently. The orientation of the dendrites was changed by the heat flow to the surrounding atmosphere. Microcracks were mainly found in between the dendrites and only few were found in the main branches. Here, a microstructure consisting of spherical FeCr particles was observed. The particles were lined up in rows, and the size of the particles typically ranged from 1 to 5 μm. However, larger particles (10–20 μm) were also observed. The shape of the FeCr particles was more or less spherical but seemed to be controlled by the surrounding ceramic.

The glassy Si phase and the FeCr particles were found in interdendritic regions. The growth of the dendrites was limited by the other dendrites leaving no or only very small amounts of glassy phase in between. In some cases the Cr_2O_3 phase could be found on the outside of the dendrites. In Cr_2O_3 with 5 wt.% Si, the microstructure showed a large amount of the glassy Si phase. The dendritic solidification structure was found to have a faceted structure, indicating an unrestricted growth of Cr_3O_4 into the Si-containing liquid oxide. Despite the fact that the FeCr particles were interdendritic together with the glassy Si phase, they were in direct contact with the Cr_3O_4 and had the same orientation relationship as observed in the case of the Fe_4Cr matrix.

TEM analysis revealed that the dendrites and the interface layer have the same orientation over distances

of more than 100 μm indicating directional growth from the edge to the center of the melt pool. A preferred orientation of the close-packed $(112)_{Cr_3O_4}$ planes parallel to the interface was observed (Fig. 8). In that case the $(112)_{Cr_3O_4}$ type twins were parallel to the interface in the thin interfacial layer. In the dendrites twins were on the other $(112)_{Cr_3O_4}$ planes as well. Small orientation changes were found at the necks of the dendrites, and the twin spacings were larger than in the Fe_4Cr (Fig. 9).

In some cases very small grains (1 μm) were found on the interface having the fcc structure and having the following orientation relationship with the ceramic coating (Fig. 10): $(110)_{Cr_3O_4} // (200)_{fcc}$ and $[\bar{1}12]_{Cr_3O_4} // [011]_{fcc}$. These grains had solidified from the interface and were passed by the solidification front from the edge of the melt pool.

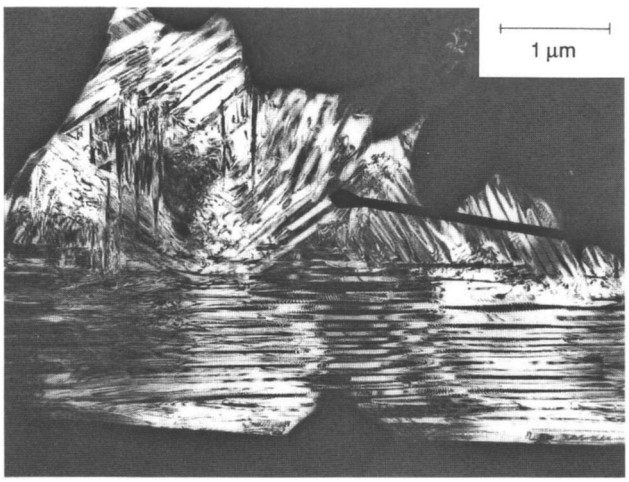

FIG. 8. Dark-field TEM image of Cr_3O_4 coating on duplex SAF 2205 showing twins parallel to the interface. In the visible part of the dendrites, twins are also on other $(112)_{Cr_3O_4}$ planes.

FIG. 9. Dark-field TEM image of Cr_3O_4 on duplex SAF 2205 showing larger twins than in Cr_3O_4 on Fe 22 wt.% Cr (Fig. 5).

IV. DISCUSSION

The crystal structure of Cr_3O_4 is tetragonal with the space group $I4_1/amd$.[6] It represents the spinel structure with the C-axis being shorter than the A- and the B-axes. In normal spinel with composition AB_2O_4, the O^{2-} ions form an fcc sublattice with A^{2+} ions in the tetrahedral interstices and B^{3+} ions in the octahedral interstices. According to the literature[7] the ionic radii of the metal ions are 0.073 nm for Cr^{2+}, 0.063 nm for Cr^{3+}, and 0.077 nm for Fe^{2+}. As the Fe^{2+} is more stable than the Cr^{2+}, it is likely that the available Fe ions will be Fe^{2+}. Because the ionic radius of Fe^{2+} is larger than that of Cr^{2+}, the lattice parameters will be elongated upon the addition with Fe. If Cr_3O_4 is compared to the cubic spinel $FeCr_2O_4$, it is observed that only the C-parameter changes substantially (10%). This is in agreement with our experiment where it is observed that the C-parameter changes 2.7% and the A- and B-parameters change 0.2%.

According to the literature[8] Cr_3O_4 is a high temperature phase which decomposes eutectoidally into Cr_2O_3 and α–(Fe, Cr) at a temperature of 1500 °C. One reason for low temperature existence of the Cr_3O_4 structure is the stabilization by 4 at.% Fe and in the case of the duplex SAF 2205 by Mn. The other reason is the cooling rate in the order of 4.10^5 °C/s which is too high for the decomposition to occur. This cooling rate can be obtained from the laser speed of 20 mm/s combined with a measured temperature difference of 700 °C over 35 μm, indicating an average temperature change of 2.10^7 C/m and 4.10^5 °C/s in the temperature range from 2200 to 1500 °C at the metal–Cr_3O_4 interface.

At a composition of $Fe_{0.5}Cr_{0.5}$ according to the Fe–Cr phase diagram,[9] the σ-phase forms congruently from the α-phase at 830 °C and decomposes eutectoidally at 440 °C to iron-rich bcc and chromium-rich bcc. It is found that in the Cr_3O_4 coating the FeCr particles all have the bcc structure and in TEM no decomposition could be detected. This suggests that no transformation to the σ-phase has occurred which is probably due to the extremely low rate of nucleation of this phase.[8]

A. Formation of the ceramic coating

The formation of the ceramic coating can be understood by an analysis of the Fe–Cr–O ternary phase diagram.[10] However, it should be kept in mind that it represents an equilibrium phase diagram and is therefore inadequate to represent some of the rapid thermal changes taking place during laser treatment. It is assumed that the reaction times are large enough for liquid state reactions to reach equilibrium. The basis for this assumption is the fact that the size of the melt pool is about 800 μm; i.e., with a laser velocity of 20 mm/s the material is about 1/25 s in the molten state. The 75% of

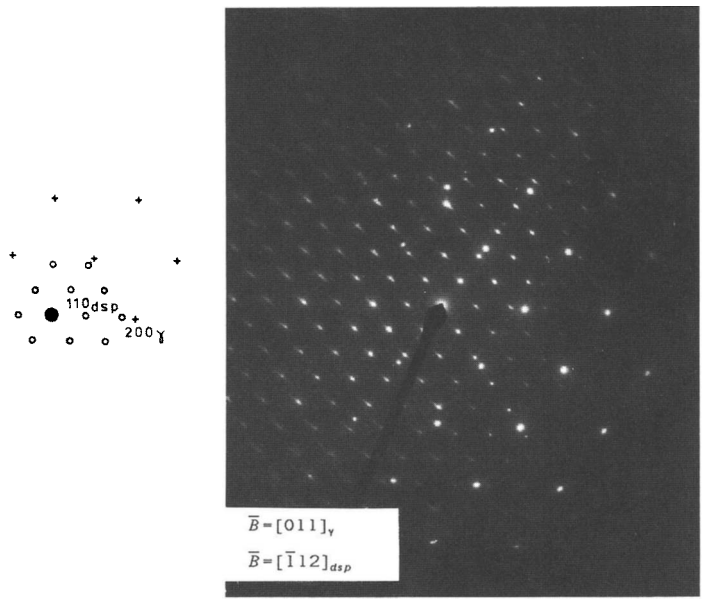

FIG. 10. Electron diffraction pattern of fcc-iron particle on the interface having an orientation relationship with Cr_3O_4. $(110)_{Cr_3O_4} // (200)_{fcc}$ and $[\bar{1}12]_{Cr_3O_4} // [011]_{fcc}$.

overlap between succeeding laser tracks results in a total interaction time in the order of 1/6 s. Good mixing in the melt pool is obtained by a strong convection in the melt pool caused by surface tension gradients. These surface tension gradients are caused by the large temperature differences in the melt pool.

The liquidus projection of the Fe–Cr–O phase diagram (Fig. 11)[11] indicates a phase separation in the liquid state resulting in a metal-rich liquid L_m and an oxygen-rich liquid L_o. The density of the L_m is 7.8 g/cm^3 [12] and of the L_o is 5.2 g/cm^3,[2,13] resulting in an L_o floating on top of an L_m. The two liquid phases formed during melting, $Metal_{liq}$ and $(Cr_2O_3)_{liq}$, are not in equilibrium resulting in a diffusion of oxygen into the molten metal and diffusion of Fe and Cr into the molten Cr_2O_3. The

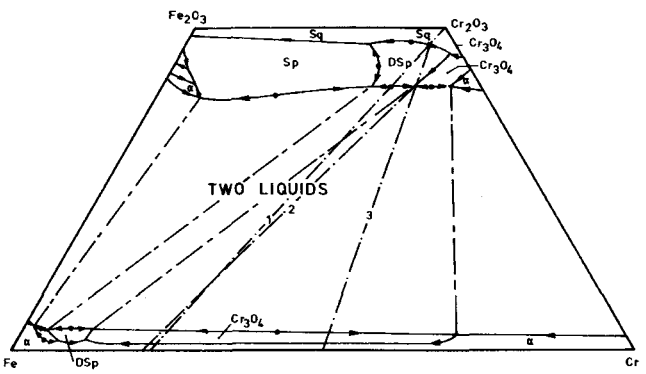

FIG. 11. Cr–Fe–O schematic liquidus projection. (1) Line of overall starting composition, (2) line of phase separation in the liquid state, and (3) line of decomposition of the liquid coating material into Cr_3O_4 and α–FeCr.

equilibrium liquids are an L_m with the composition of the original metal containing 3 at. % O and an L_o containing 50 at. % O, 40 at. % Cr, and 10 at. % Fe (in between C1 and M2 on the liquidus projection). Because of the strong convection described above, the L_o is swept to the side of the melt pool causing the ceramic coating to be thicker at the edge of the melt pool and making it necessary to have sufficient overlap between succeeding tracks.

The solidification rate is so high that there is no further interaction between the L_m and the L_o during cooling which as a result solidify as two independent liquids. The L_m solidifies into a metal having the same composition and phases as the unlasered steel, only the grains are much smaller due to the much higher quenching rates during laser treatment. The 3 at. % O in the L_m results in a small fraction of Cr_3O_4 particles in the matrix.

The L_o decomposes by a monotectic reaction into $Fe_{0.3}Cr_{2.7}O_4$ and L_m with composition FeCr. According to the tie lines in the phase diagram, decomposition should result in Cr_3O_4 and L_m with composition Fe_4Cr. Thus, we may conclude that the cooling rate is too high for an equilibrium decomposition to occur. It is found that the composition of the two observed phases and the L_o are on one tie line. By the lever rule the decomposition should result in 85 vol. % Cr_3O_4 and 15 vol. % FeCr. Measurements of surface fraction FeCr indicate the coating contains between 8 and 11 vol. % FeCr. The reason for this deviation could be a nonequilibrium situation due to the continuous addition of Cr_2O_3 to the coating. Further, a systematic error in the measured volume fraction may arise due to pushing out of the FeCr particles.

B. Microstructure of the ceramic coating

The process of a continuous heat source scanning over a surface results in continuous melting at the front of the melt pool and continuous solidification at the rear edge of the melt pool. This results in a continuous growth at the rear edge of the melt pool without a nucleation problem. This is indeed observed in the Cr_3O_4 ceramic coating. Because the L_o with a higher melting point is floating on top of the L_m with a lower melting point, solidification first occurs on the L_o side of the L_o–L_m interface resulting in a ceramic film floating on top of the L_m and effectively separating the L_o from the L_m. This process is possible because the monotectic temperature of the reaction $L_o \rightarrow Cr_3O_4 + L_m$ (at 1660 °C) is only 150 °C above the solidification temperature of Fe 22 wt. % Cr so that the ceramic film advances only 10 μm into the liquid (Fig. 12). Upon this initial thin film the rest of the coating solidifies. Now we have to consider the effect of Si on the microstructure in the coating.

Without Si in the L_o the solidification from the film is a directional solidification process with a flat interface in which the interface is following the temperature gradient in the melt. Because the L_o solidifies by the monotectic reaction described above, there is a continuous saturation of the L_o with Cr and Fe at the solidification front. This results in a phase separation, i.e., nucleation and growth of L_m droplets in the L_o. In order to minimize the surface free energy the shape of these particles is spherical, but the advancing solidification front makes the particles elliptical. Thus, the results indicate that the nucleation and growth of the L_m is a rapid enough process not to disturb the growth of the Cr_3O_4.

This flat interface solidification process results in a dense and homogeneous ceramic coating. The problem with this coating lies in the tensile stresses generated during laser treatment. Due to the extremely large thermal gradients during cooling (in the order of 1.10^8 °C/m in the ceramic, as will be estimated below), a large amount of thermal stress is generated in the coating resulting in the microcracking visualized by etching. These microcracks form networks through the coating deteriorating the mechanical stability of the coating during subsequent processing.

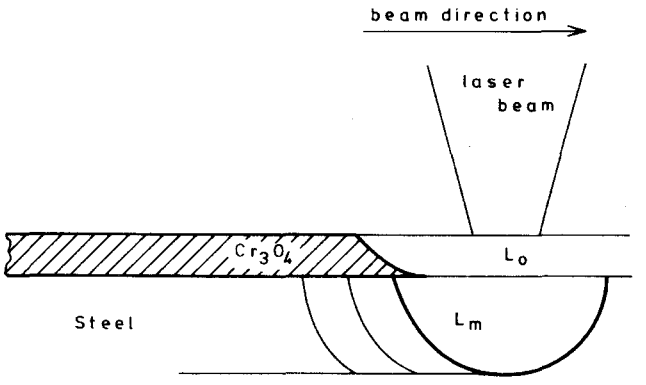

FIG. 12. Schematic longitudinal section of a laser track. Because of the higher solidification temperature of the Cr_3O_4, the coating sticks into the melt pool.

The presence of Si in the L_o results in a structure of vertically oriented dendrites in the ceramic coating growing on the interfacial layer. This structure resembles the columnar structure found to be very useful for thermal barrier coatings.[15] As the microcracks are mainly found in between the dendrites and not in the main branches, this microstructure has less change of mechanical failure by interconnecting networks of cracks.

Because the dendrites must follow the temperature gradient in the L_o and they make very small angles with the interface, it can be reasoned that the heat flow is mostly through the metal. Cooling through the ceramic is of importance only at the sides of the laser pool, and the dendrites are oriented differently. This is in agreement with the thermal conductivity data of 21 W/m · K (at 400 °C)[1] for the duplex and 2 W/m · K (at 150 °C) (estimated from spinel data in Ref. 14) for the Cr_3O_4. The heat capacity c_p of both materials is 600 J/kg · K.[1,13] The tilt of the dendrites with respect to the movement of the laser beam can, in the stationary case, be used to calculate the growth velocity of the dendrites. The laser velocity of 20 mm/s combined with the growth angle of 10° results in a growth velocity $V = 20.10^{-3} \sin 10°$ m/s.

The tilt of the dendrites combined with the measured temperature gradient at the interface of 2.10^7 °C/m can be used to estimate the temperature gradient in the ceramic. The problem is that besides the solidus line no other temperature lines are known in the ceramic. The temperature gradient G_T in the ceramic should, however, be smaller than the projection of this gradient on the growth direction of the dendrites:

$$G_T < 2 \cdot \frac{10^7}{\sin 10°} [°\mathrm{C/m}]. \qquad (1)$$

The requirement for interface stability can be used to calculate the maximum diffusion coefficient for Si in the L_o for which a dendritic structure would be expected. A sufficient condition for stability of the interface in directional solidification is[16]:

$$\Delta C \cdot \frac{V}{D_{Si} \cdot G_T} < \left| \frac{\delta C_L}{\delta T} \right| \qquad (2)$$

where

$\Delta C = C_L^0 - C_S^0$ = concentration in liquid minus concentration in the solid,

V = velocity of temperature field,

G_T = $\delta T/\delta z$ = temperature gradient in the growth direction, and
$\delta C_L/\delta T$ = change of liquidus temperature with concentration and $\delta C_L/\delta T = \Delta C/\Delta T$.

ΔT is taken to be 160 °C because only occasionally segregation of Cr_2O_3, which occurs below 1500 °C, is found, indicating that the growth process takes place between 1500 °C and the monotectic decomposition temperature of 1660 °C. Substitution of the appropriate values for G_T and V predicts that diffusion coefficient for dendritic growth is $D_{Si} < 5 \cdot 10^{-9}$ m^2/s. Diffusion data for Fe in molten FeO–SiO_2 at 1275 °C rescaled to Si give $8 \cdot 10^{-10}$ m^2/s.[17]

From the above data it can be calculated whether the dendritic structure is stable and if so what the interdendritic spacing will be. In this calculation it is essential that the thermal diffusion coefficient l_T is larger than the solute diffusion coefficient l_D in order for the solute diffusion to be the rate limiting and destabilizing factor. The calculated interdendritic spacing λ should be larger than l_D so that the growing dendrites do not interact through material diffusion and side branches can be formed. The dendritic structure is stable if $l_D < \lambda < l_T$, where $l_T = \Delta C/G_T \cdot |\delta T/\delta C_L| \approx \Delta T/G_T = 1.4 \cdot 10^{-6}$ m$l_D = 2 \cdot D_{Si}/V = 4.5 \cdot 10^{-7}$ m, leading to $\lambda \sim \sqrt{l_T \cdot l_D} = 1 \cdot 10^{-6}$ m. The calculated λ provides an approximation of the lower limit of the dendritic spacing (Fig. 6). The broadening of the dendrites is an indication that the temperature gradient G_T is smaller near the top of the coating.

As can be seen from the formulae, there is a relation between the interdendritic spacing λ and the velocity of the temperature field V : $\lambda^2 \cdot V$ = constant. This equation suggests a relation between the laser velocity v and the interdendritic spacing, but this relation is obscured by the dependence of the temperature field on the laser velocity. Actually, this will lead to an equation like $\lambda^m \cdot V$ = constant, where $m < 2$.[18]

V. CONCLUSIONS

After laser coating steel containing 22 wt. % Cr with Cr_2O_3, the Cr_2O_3 powder has completely transformed to $Fe_{0.3}Cr_{2.7}O_4$ having the tetragonal distorted spinel structure. Dispersed in the coating are metallic particles with composition FeCr and a bcc structure. The phases in the coating can be explained from the Fe–Cr–O equilibrium phase diagram with the assumption that complete phase equilibrium is reached in the liquid state but not during solidification. The two equilibrium phases, L_o and L_m, that exist in the molten state, solidify as two independent liquids.

No crystallographic orientation relation is observed between the steel matrix and the Cr_3O_4 coating although the $(101)_{Cr_3O_4}$ close-packed plane is in most cases parallel to the interface. This indicates a different solidification history for the matrix, solidifying from the bottom of the melt pool, and for the Cr_3O_4 coating, solidifying from the edge of the melt pool. An orientation relation is always observed between the Cr_3O_4 coating and the FeCr particles in the coating.

When no Si is present in the Cr_3O_4 coating, no solidification structure is found in the coating and the FeCr particles are randomly dispersed in the coating. Although this type of coating is homogeneous, the temperature shock during cooling results in a dense network of microcracks. When Si is present in the Cr_3O_4 coating, either from the ceramic powder or from the steel matrix, a dendritic growth structure is produced. Only the primary arms of the dendrites are developed. In between the dendrites is a glassy phase containing Si. FeCr particles are also interdendritic. Due to the higher thermal conduction coefficient of the matrix, the dendrites are oriented vertically in the coating resulting in a columnar structure. In this type of coating the cracks are mostly in between the dendrites. The formation of the dendrites can be explained from solidification theory using the experimental data for thermal diffusion and Si diffusion in the L_o.

ACKNOWLEDGMENT

This work is part of the research program of IOP-Metalen (C89 427 RG XX), The Hague, The Netherlands and of the Foundation for Fundamental Research on Matter (FOM-Utrecht), and has been made possible by financial support from the Netherlands Organization for Research (NWO-The Hague).

REFERENCES

1. "Sandvik SAF 2205", UNS S31803, Sandviken, Sweden, S-1, 874-ENG (1989).
2. JCPDS 12-559; D. C. Hilty, W. D. Forgeng, and R. L. Folkman, Trans. Am. Inst., Min. Metall. Eng. **203**, 253 (1955).
3. *Metals Handbook, Metallography and Microstructures* (American Society for Metals, Metals Park, OH, 1985), Vol. 9, p. 282.
4. Philips APD 1700 system.
5. X. B. Zhou and J. Th. M. De Hosson, Acta Metall. **39**, 2267 (1991).
6. C. Palache, H. Berman, and C. Frondel, *Dana's System of Mineralogy* (John Wiley, New York, 1946), Vol I, p. 712.
7. W. D. Kingery, *Introduction to Ceramics* (John Wiley, New York, 1967), p. 58.
8. M. Hansen and K. Anderko, *Constitution of Binary Alloys* (McGraw-Hill, New York, 1958).
9. O. Kubaschewski, *Iron-Binary Phase Diagrams* (Springer-Verlag, Berlin, 1982), pp. 31–34 (Review).
10. V. Raghavan, *Phase Diagrams of Ternary Alloys, Part 5, Ternary Systems Containing Iron and Oxygen* (Indian Institute of Metals, New Delhi, India, 1989), p. 89.
11. D. C. Hilty, W. D. Forgeng, and R. L. Folkman, Trans. Am. Inst., Min. Metall. Eng. **203**, 253 (1955).

12. *American Institute of Physics Handbook*, Am. Inst. of Physics (McGraw-Hill, New York, 1972), pp. 2–24.
13. G. V. Samsonor, *The Oxide Handbook* (Plenum, New York, 1973), pp. 34, 144.
14. *Handbook of Chemistry and Physics*, 52nd ed., E5 (CRC Press, Cleveland, OH, 1972).
15. K. Fritscher and W. Bunk, Density Graded TBC's Processed by EB-PVD, 1st Int. Symp. Functionally Gradient Material, Oct. 1990, Sendai, Japan.
16. W. Mullins and R. Sekerka, J. Appl. Phys. **34**, 323 (1963).
17. Diffusion and Defect Data **4**, 100 (1970).
18. H. Müller-Krumbhaar and W. Kurz, in *Materials Science and Technology*, edited by R. W. Cahn, P. Haasen, and E. J. Kramer (VCH Publishers, Inc., New York, 1991), Vol. 5, p. 553.